ADVANCING EARTH AND SPACE SCIENCES

JGR Atmospheres

RESEARCH ARTICLE
10.1029/2023JD038549

Key Points:
- Tropical gravity wave signatures are identified in superpressure balloon observations and storm-resolving models
- Adjustment of the low pass filtering time for the observational data allows sampling balloons as models
- Gravity wave amplitudes decay with distance to closest deep convection, their main source in the tropics

Correspondence to:
L. Köhler,
laura.koehler@mpimet.mpg.de

Citation:
Köhler, L., Green, B., & Stephan, C. C. (2023). Comparing Loon superpressure balloon observations of gravity waves in the tropics with global storm-resolving models. *Journal of Geophysical Research: Atmospheres*, *128*, e2023JD038549. https://doi.org/10.1029/2023JD038549

Received 18 JAN 2023
Accepted 11 JUL 2023

Comparing Loon Superpressure Balloon Observations of Gravity Waves in the Tropics With Global Storm-Resolving Models

Laura Köhler[1], Brian Green[2], and Claudia C. Stephan[1]

[1]Max Planck Institute for Meteorology, Hamburg, Germany, [2]Department of Earth System Science, Stanford University, Stanford, CA, USA

Abstract Superpressure balloons, which drift approximately on isopycnal surfaces, get displaced by gravity waves and are thus capable of detecting gravity wave signatures. The project Loon provides superpressure balloon data in the upper troposphere and lower stratosphere from 2011 to 2021. We compare Loon data from the 6 years of best data coverage with output of global storm-resolving models from the DYnamics of the Atmospheric general circulation Modeled On Non-hydrostatic Domains winter initiative in the tropics. We study the variance of the vertical velocity and, for the models, the gravity wave momentum flux as function of distance to closest convection. The models show large differences in the variance of the vertical wind velocity, which is crucial for calculating vertical gravity wave momentum fluxes. We find large differences between the models with respect to simulated convection, lateral propagation, and the wave background away from sources. We then sample balloons as models by optimizing the match of vertical wind distributions using a temporal low pass filter. The average distance the balloons travel during the optimum low pass filtering time turns out to correspond approximately to four times the model grid spacing. The functional dependence of the vertical velocity variance on distance to closest convection is similar between the models and the observations sampled as models. The robustness of this result across all models suggests that storm-resolving models provide a useful resource for machine learning some characteristics of convectively generated gravity waves.

Plain Language Summary Superpressure balloons drift on surfaces of constant density in the upper troposphere and lower stratosphere. The balloons get displaced by gravity waves and are thus capable of measuring their signatures. We compare superpressure balloon observations from the project Loon, a commercial project which was intended to provide internet access to remote regions, to high-resolution models from the DYnamics of the Atmospheric general circulation Modeled On Non-hydrostatic Domains winter initiative in the tropics. We investigate the variance of vertical wind and the gravity wave momentum flux as function of distance to closest convection, the main source of gravity waves in the tropics. To sample balloons as models we use a temporal low pass filter. Despite large differences in gravity wave amplitudes, we find similar characteristics in models and observations which is promising for potential machine learning applications to understand the underlying physics.

1. Introduction

Gravity waves from tropospheric sources, such as convection and orography, transport momentum across the atmosphere and therefore influence weather and the climate system on multiple scales. Many studies examined the effects of gravity waves on large-scale circulation, such as the quasi-biennial oscillation (Alexander & Holton, 1997; Anstey et al., 2016) and sudden stratospheric warmings (Stephan et al., 2020; Watanabe et al., 2022). Other previous studies focused on the interaction of gravity waves with tropospheric phenomena, such as cirrus clouds (Dinh et al., 2016; Jensen et al., 2016) and turbulence (Callies et al., 2014; Sharman & Trier, 2019). Validating the realism of gravity waves simulated by numerical models still poses major challenges. In low resolution models, gravity waves are typically parameterized, whereas they are explicitly resolved in high resolution storm-resolving models. Even in the latter class of models it remains unclear at which resolution the gravity wave spectrum is sufficiently well resolved (Polichtchouk et al., 2022).

A relatively novel idea for improving parameterizations employs machine learning methods (Espinosa et al., 2022). This requires one to assess how well storm-resolving models simulate gravity waves since their output is typically used as training data for neural networks. Faith in the machine learning approach toward improving parameterizations depends on the realism of simulated lateral propagation and convective sources (Stephan et al., 2022). Comparing storm-resolving models to observations is useful for informing us how model output can be used as training data. Moreover, it may shed light on the physical processes related to the generation and propagation of gravity waves, which storm-resolving models represent physically albeit differently. The goal of this work is to study how global storm-resolving models simulate the amplitude of gravity waves in the tropics compared to observations.

On the observational side, gravity waves have been studied with a large variety of measurement techniques such as space-borne remote sensing (Chen et al., 2022; Miller et al., 2015), radiosondes (Hindley et al., 2021), lidars (Banyard et al., 2021), aircraft measurements (Atlas & Bretherton, 2022), and superpressure balloons (Corcos et al., 2021; Nastrom, 1980; Vincent & Hertzog, 2014). Superpressure balloons have a diameter between 10 and 20 m, are filled with a lifting gas, usually helium, and drift in the upper troposphere or lower stratosphere on isopycnal surfaces for months. Their trajectories get distorted by gravity waves which is reflected in their position and in the temperature and pressure data. Data from the French-US Strateole-2 campaign (Haase et al., 2018) have been intensively used to study gravity waves (Cao et al., 2022; Corcos et al., 2021; Lott et al., 2023). In this study, we use Loon superpressure balloon observations.

Loon (Rhodes & Candido, 2021) was a commercial project intended to improve global internet coverage, launching superpressure balloons into the lower stratosphere from 2011 to 2021. The balloons measure temperature and pressure, their position is determined via GPS. Compared to scientific campaigns such as Strateole-2, a unique characteristic of the Loon balloons was their vertical maneuvering, which results in gaps in the data. Yet, Loon provides measurements from several years with extensive data coverage. The data will be introduced in more detail in Section 2.1.

For simulated data, we use output from the DYnamics of the Atmospheric general circulation Modeled On Non-hydrostatic Domains (DYAMOND) winter initiative (Stevens et al., 2019). DYAMOND has been designed to compare different storm-resolving models and provides simulations for 40 days in January and February 2020 (see Section 2.2 for further information).

Balloon observations are special in that they provide localized information on gravity waves, as opposed to, for instance, satellite measurements, which have a limited vertical resolution (Stephan et al., 2019a, 2019b). When comparing superpressure balloon observations to storm-resolving models, we have to account for the fact that balloons sample the atmosphere along trajectories whereas model output comes on grids and is only available at relatively large output time intervals. Models have an effective resolution which determines the minimum wavelength they can resolve. By applying a low pass filter to the balloon data, we reduce their resolution to sample them as models. In Section 3.1, we discuss the filtering times that correspond to the models' effective resolutions.

To study gravity waves in models and observations, we link gravity waves to their potential sources similarly to Corcos et al. (2021). In that paper, the authors studied gravity waves in the Strateole-2 data by looking at different quantities such as momentum flux and temperature variances as a function of distance to closest convection, a major source of gravity waves. In Section 3.2, we consider the variance of the vertical wind velocity w in a similar way, since in the absence of convection w is dominated by gravity waves. In Section 3.3, we determine the gravity wave momentum flux for the DYAMOND winter models. We study mean and variance of the momentum flux as function of distance to closest convection, as before. We conclude with a summary and outlook in Section 4.

2. Observational Data and Models

2.1. Loon Superpressure Balloon Data

Loon (Rhodes & Candido, 2021) was a commercial project intended to provide internet access to remote regions. For this purpose, superpressure balloons were released to drift in the upper troposphere and lower stratosphere. The balloons provide their GPS position, ambient temperature, and pressure along their trajectories. In the scientific context, the Loon data have been used to study the inertial peak in the stratospheric wind spectrum (Conway et al., 2019) and the gravity wave spectrum (Lindgren et al., 2020; Schoeberl et al., 2017).

The balloons follow Lagrangian air motions and thus one can extract the wind from the GPS position. Data is sampled in timesteps of 60 s. The error for the temperature measurements is ±5 K. The pressure comes with an error of ±1 hPa. The horizontal and vertical GPS position is given with an accuracy of ±2.5 m. The balloons are

10.1029/2023JD038549

actively maneuvered in height for navigation. Balloons were flown from 2011 to 2021; here we use data from 2014 to 2019. In this time interval, around 1,400 flights took place. Flight segments between identified maneuvering events last from hours to months. There is no data coverage in high latitude regions and over Eurasia (cf. Figure 1 in Lindgren et al. (2020)). For the following analysis, we use the complete data set without time restrictions, like choosing the same period as in the models, to maximize the number of balloon flights for statistical analysis. Outside the maneuvering periods, the balloons drift approximately on isopycnal surfaces at heights between 16 and 21 km. The mean pressure of the Loon data is approximately 70 hPa, which is used to guide the comparison to numerical output.

We did some processing of the raw data before analyzing it, to identify and remove balloon maneuvering and to interpolate the data onto equal time steps. First, maneuvering in a balloon flight is identified by examining gaps in the data larger than 5 min. Two criteria must be met for a data gap to be identified as a maneuvering event. The first is the magnitude of the altitude jump across the gap must exceed 100 m. The second is the mean altitudes of the two data "chunks" (continuous data without any gaps) on either side of the gap must be different by more than three times the average of their standard deviations. If both criteria are met, the flight is split into segments on either side of the gap and the segments are analyzed separately. Comparison with a newer version of the Loon data set which includes an "Altitude Control System" flag confirms that our algorithm manages to identify maneuvering gaps reliably. We randomly tested the sensitivity of our results on the exact edges of the maneuvering gaps to check that this does not affect the results. The balloons typically record GPS data every 60 s, but the time between data points varies, so all the data for each segment are interpolated onto evenly spaced 2-min intervals.

The vertical velocity can be calculated from the altitude or from the pressure assuming hydrostatic equilibrium and making use of the ideal gas equation. However, the accuracy of the latter method is restricted by the large errors of temperature and pressure provided by Loon. Furthermore, some segments lack valid temperature data. Thus, we use the first approach and calculate the vertical velocity of the balloon w_{balloon} from the altitude information. For the derivative, we use the central difference, that is,

$$w_{\mathrm{balloon}}(t) = \frac{dz(t)}{dt} \approx \frac{z(t+\Delta t) - z(t-\Delta t)}{2\Delta t}. \tag{1}$$

As pointed out in Massman (1978), Nastrom (1980), Boccara et al. (2008), and Vincent and Hertzog (2014), we have to account for the fact that the balloons drift on isopycnal surfaces whereas air parcels move on isentropes. For sufficiently slow motions on time scales longer than twice the Brunt-Väisälä period, this just requires a constant correction factor for vertical displacements Δz, namely $\Delta z_{\mathrm{balloon}} = \alpha \Delta z_{\mathrm{air}}$ with $\alpha = 0.3$ (Podglajen et al., 2016). Thus, to determine the air's vertical velocity w from the balloon's vertical motion, we use $w = w_{\mathrm{balloon}}/0.3$.

The balloons start to oscillate around their density level when displaced from equilibrium. Thus, the balloon's eigenfrequency provides a lower bound on vertical air motions that can be resolved. This frequency is of the same order as the Brunt-Väisälä frequency. Therefore, we apply a low pass filter to the balloon data with different filtering times, starting with a minimum filtering time T of 15 min (Vincent & Hertzog, 2014). For our analysis, we restrict ourselves to latitudes between $-20°$ and $20°$ and only include segments between maneuvering gaps longer than 10 times the filtering time which leaves us with more than 10^4 segments. We thereby assume a spatially homogeneous distribution of the balloons. We will further discuss the value of T below in Section 3.1.

A balloon only measures the projection of a wave onto its trajectory. Therefore, to extract gravity wave momentum fluxes from the balloon data, one needs to perform a wavelet analysis (Boccara et al., 2008; Corcos et al., 2021). Here, we focus instead on the vertical velocity, which is directly available from observations and models, and its variance as a measure for gravity waves since w is nearly completely driven by gravity waves (Morfa & Stephan, 2023).

2.2. High-Resolution Models

We compare Loon data to high-resolution models from DYAMOND winter. The DYAMOND initiative (Stevens et al., 2019) was designed in 2017 to compare storm-resolving models. DYAMOND provides output from various global high-resolution models which allows investigating a large variety of questions relying on a good representation of deep convection, for instance cirrus clouds (Nugent et al., 2022), cloud organization (Christensen & Driver, 2021), tropical cyclones (Judt et al., 2021), and gravity wave momentum fluxes (Stephan et al., 2019b). Two time periods, each 40 days long, were simulated: DYAMOND summer starts on 1 August 2016 and DYAMOND winter covers the 40 days from 20 January to 1 March 2020.

In this study, we restrict ourselves to the DYAMOND winter simulations. An overview of all models involved in DYAMOND can be found here: https://easy.gems.dkrz.de/DYAMOND/. We include the following models which provide online output of the vertical velocity w, such that no hydrostatic balance has to be assumed to determine w from the pressure velocity ω. We state the vertical resolution of the models at 70 hPa which is approximately the mean pressure of the Loon data.

- ICON-NWP 2.5 km: The Icosahedral Nonhydrostatic Weather and Climate Model (ICON) co-developed by the German weather service and the Max Planck Institute for Meteorology was run with the numerical weather prediction physics schemes and with a 2.5 km horizontal resolution in an atmosphere-only setup. The output is given on 90 terrain following vertical model levels with a resolution of 650 m at 70 hPa and horizontally on the icosahedral native ICON R02B10 grid presented, for example, in Zängl et al. (2015).
- GEOS 3 km: The Goddard Earth Observing System (GEOS) model by NASA was run in an atmosphere-only setup at a 3 km horizontal resolution. The output is given on 181 sigma surfaces with 3.1 hPa resolution at 70 hPa. For further information on the model see Putman and Lin (2007).
- NICAM 3.5 km: The non-hydrostatic icosahedral atmospheric model (NICAM) by the Japan Agency for Marine-Earth Science and Technology was run with 3.5 km resolution and an atmosphere-only setup. The output is provided on 78 height levels with a level spacing of ∼400 m at 70 hPa. Detailed model information is given in Tomita and Satoh (2004).
- SHiELD 3 km: The GFDL experimental system for high-resolution prediction on earth-to-local domains (SHiELD) model by NOAA was run with an atmosphere-only setup and with a 3 km horizontal resolution. The output is given on 79 pressure levels with a resolution of ∼7 hPa at 70 hPa. Further information can be found in Harris et al. (2020).
- IFS 4 and 9 km: The Integrated Forcast System (IFS) model by ECMWF was run coupled to land, wave, and ocean with 4 and 9 km horizontal resolution, respectively. The output is computed on 137 pressure levels with 15 hPa vertical output resolution for the hourly data at 70 hPa. ECMWF (2020) presents documentation of the IFS model.

The temporal output resolution of the 3d fields is 1 hr for GEOS 3 km, IFS 4 and 9 km, and 3 hr for ICON-NWP 2.5 km, SHiELD 3 km, and NICAM 3.5 km, respectively. For analyzing the dependence on distance to convection, we consider hourly means of the precipitation rates which are computed from the total precipitation provided with 15 min temporal resolution if not directly available.

For the vertical wind comparison in Sections 3.1 and 3.2, we use w and precipitation rates on the native grids to avoid reducing gravity wave amplitudes by remapping. When considering the gravity wave momentum flux in Section 3.3, we need remapped output on a Gaussian grid to apply a Helmholtz decomposition. Therefore, we remap all wind components, temperature, and pressure (for those models that do not use pressure as the vertical coordinate) to a Gaussian N1024 grid. The Helmholtz decomposition separates the horizontal wind field into its rotational and divergent components (Lindborg, 2015). By setting the rotational part to zero, we are approximately left with the gravity wave contribution to the horizontal wind field, which is given by its divergent part (Bühler et al., 2014). After remapping back to the Gaussian N1024 grid, we use the mean over a square area with edge length of 700 km for defining perturbations and background.

We consider three pressure levels, 20, 70, and 500 hPa. We avoid vertical interpolation to maintain maximum gravity wave amplitudes. We therefore use the respective model level closest to the considered pressures. This applies to ICON-NWP, GEOS, NICAM, and SHiELD. Only IFS provides output at the studied pressures.

To compare model output on global grids with a coarser spatial and temporal output resolution than the balloon data measured on Lagrangian trajectories, we randomly distribute points in the models without calculating trajectories. These random points are located within a latitudinal range from −20° to 20°. For each model, we distribute more than 10^5 random balloon points in total.

3. Results

3.1. Low Pass Filtering Time for Loon

To remove balloon oscillations that cannot be distinguished from high frequency waves, we apply a temporal low pass filter. We cut all frequencies smaller than a cutoff frequency $\hat{f}_{\mathrm{cutoff}} = 1/\hat{T}$ with $\hat{T}$ being the filtering time in

10.1029/2023JD038549

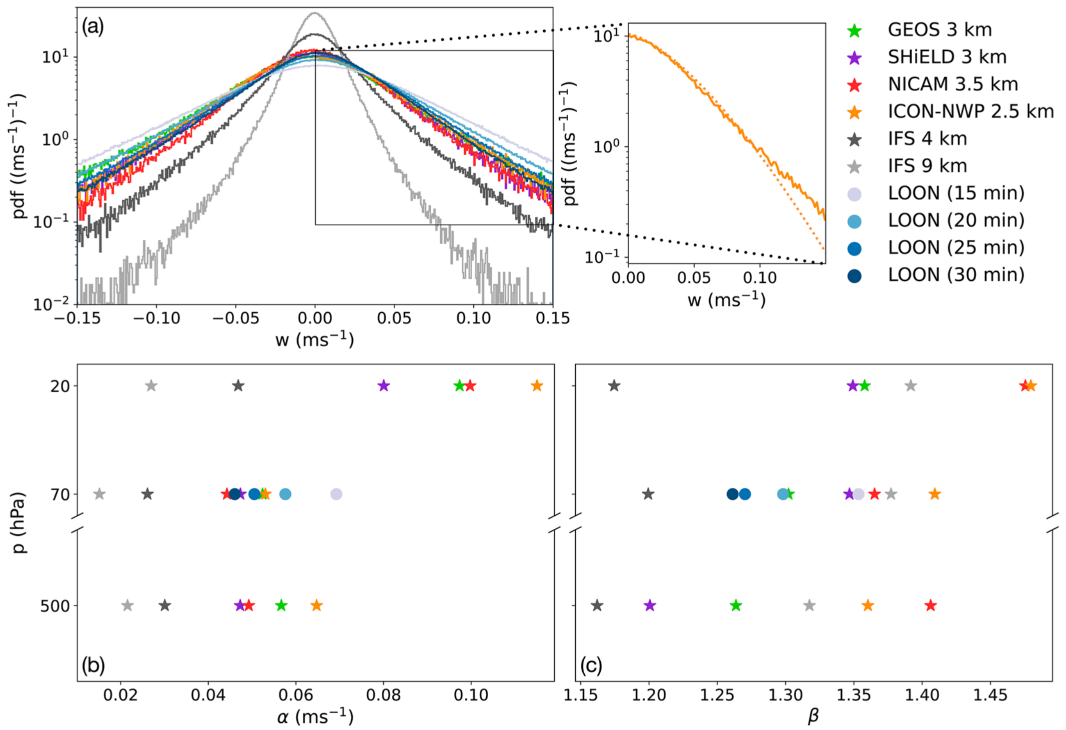

Figure 1. w is distributed approximately like a stretched exponential. (a) Shows the w distributions for the DYnamics of the Atmospheric general circulation Modeled On Non-hydrostatic Domains (DYAMOND) winter models and Loon with different filtering times at 70 hPa. The inset presents one example of a fit for ICON-NWP. The dotted line shows the fit. The fit parameters (b) α and (c) β of the stretched exponential distribution according to Equation 2 are presented at three different pressure levels. Stars denote the DYAMOND winter models according to the legend and the blue circles represent the Loon data with different filtering times.

the moving balloon frame. To remove the balloon oscillations, the filtering time needs to be larger than at least 15 min (Corcos et al., 2021). Applying a low pass filter corresponds to smoothing the balloon data measured on trajectories. On the other hand, the model output has limited spatial resolution. We suggest to use the low pass filter on the trajectories additionally to removing the balloon's intrinsic oscillations to find a filtering time which corresponds to the effective spatial resolution of the models. For simplicity, we assume that the balloons move relatively slowly compared to gravity wave phase speeds, and thus neglect Doppler shifts for the following comparison between moving balloon frames and static global model frames. This corresponds to assuming $T = \hat{T}$. We therefore drop the hat in the following.

We compare the probability distribution functions (pdf) of the vertical wind velocity w for the different models and the Loon data with different filtering times as presented in Figure 1a. We find that the pdfs for w follow approximately normalized stretched exponential distributions (Podglajen et al., 2016), also called double exponential or symmetric generalized normal distributions, that is,

$$p(w) = \frac{\beta}{2\alpha\Gamma(1/\beta)} \exp\left[-(|w-\mu|/\alpha)^{\beta}\right], \tag{2}$$

where α and β are free parameters, μ is the mean value, which is assumed to be zero for w, and $\Gamma(x)$ is the gamma function. β ranges between 1.1 and 1.5 and parameterizes the transition from a Laplacian ($\beta = 1$) to a Gaussian ($\beta = 2$) distribution. α is a scale parameter. In the case of $\beta = 2$ it corresponds to $\sqrt{2}$ times the standard deviation. The inset in Figure 1a presents the fitted stretched exponential (dotted line) to the pdf (solid line) exemplary for ICON-NWP 2.5 km. It covers the behavior at sufficiently small $|w|$ very well but misses the tail with higher occurrence frequencies of large $|w|$ present in the models as well as in the Loon data.

The width of the w distribution of Loon decreases with increasing filtering time. We find that the observational w distribution with a filtering time of 15 min, shown by the lightest blue histogram in Figure 1a, is much broader than the models' distributions. When we increase T, shown in darker blue, the pdf gets steeper and we approach a distribution similar to those of the models. Note that the only fitting parameter is the filtering time T. Both $\alpha(T)$ and $\beta(T)$ depend on T. Thus, although decreasing β alone would lead to a broadening of the distribution, fitting T to a steeper curve leads to a decrease of both $\alpha(T)$ and $\beta(T)$. Figure 1b presents the fit parameter α and Figure 1c presents β, respectively, of the models (stars) at three different pressure levels and of Loon at 70 hPa with different filtering times (blue dots). β decreases for Loon from 1.35 to 1.26 when increasing the filtering time from 15 to 30 min. α decreases from 0.07 to 0.05 m s^{-1}. The combination of both leads to a narrowing of the distribution. In terms of least squares error we find the best agreement with ICON-NWP 2.5 km for a filtering time $T = 25$ min, for GEOS 3 km, we get $T = 23$ min. For SHiELD 3 km, the best fit is obtained for $T = 28$ min and for NICAM 3.5 km for $T = 30$ min, respectively. Within the considered range of filtering times for Loon between 15 and 30 min, we find the best agreement with both IFS resolutions for $T = 30$ min. However, as seen in the pdfs in Figure 1a, the IFS distributions have a much smaller width than Loon. We nevertheless restrict this analysis to filtering times up to 30 min since many Loon segments only cover time intervals of a few hours between maneuvering gaps. Longer filtering times thus reduce the number of useable segments and deteriorate the statistics. This approach does not take into account systematic errors in the models like underestimating w, which is certainly the case for IFS, but assumes that the vertical velocities in the models are correct. This assumption is supported by the following simple scaling argument.

To resolve a wave in the models, at least four grid boxes are needed. Thus, GEOS 3 km can resolve waves with wavelengths larger than ∼12 km. This value agrees nicely with the mean distance the Loon balloons travel in 23 min, which is indeed 12 km, since they have an average horizontal speed of 8.7 m s^{-1}. The agreement turns out to be reasonably good for the other models, too: ICON-NWP 2.5 km can in principle, that is, in a perfect model, resolve minimum wavelengths of ∼10 km and the balloons travel on average 13 km in 25 min, for SHiELD 3 km, the minimum wavelength is ∼12 km and the mean traveling distance in 28 min is 15 km, and for NICAM we have a minimum wavelength of ∼14 km and a mean balloon distance of 16 km, respectively. We ignore IFS here, since the agreement with Loon is worse than for the other models. Although model effective resolution is not four times the grid spacing (Skamarock, 2004), and the ratio differs between the models, our simple scaling between horizontal grid spacing and filtering time T leads to a reasonably good agreement between balloon measurements and numerical models. To compare superpressure balloon data to models, we have to exclude small waves measured by the balloons but not resolved in the models by applying a low pass filter with a sufficiently large filtering time. For further analysis, we will use a filtering time of $T = 25$ min which is consistent with most of the considered models except for IFS, especially IFS 9 km.

3.2. Variances of the Vertical Velocity

Deep convection is one of the main sources of gravity waves, especially in the tropics. Therefore, we compare variances of the vertical velocity σ_w^2 as function of distance to closest convection d between Loon and the DYAMOND winter models. The balloons correspond to points in space and time. To compare these to global models, we distribute random points in the models, which serve as virtual balloons. However, we do not calculate virtual balloon trajectories but distribute uncorrelated random "balloons" at every time step to avoid interpolation in space and time which comes with the risk of reducing wave amplitudes.

To determine the closest convection, we use the mean precipitation rate in the previous hour. To take into account only deep convection, we consider precipitation rates larger than a threshold of 6 mm hr^{-1} consistent with Bramberger et al. (2020). For the Loon observations, we use CMORPH satellite data (Joyce et al., 2004; Xie et al., 2017, 2019) which provides precipitation rates with a temporal resolution of 30 min and a spatial resolution of 8×8 km^2 at the equator. We compute hourly means of the CMORPH data as for the models.

We consider only the tropics and distances to closest convection d up to 1,000 km. Thus, we only take into account (virtual) balloons in a latitude range of −20°–20° such that convection at distances up to 1,000 km still takes place in the tropics. Figure 2 shows $\sigma_w^2(d)$ for the DYAMOND winter models at (a) 20, (b) 70, and (c) 500 hPa, respectively. At 70 hPa, Loon is included for which, as mentioned above, a filtering time of 25 min is used and all Loon data points are collected without correction for deviations from this pressure. The variances at 20 and 70 hPa follow approximately a power law in the considered distance range up to 1,000 km,

$$\sigma_w^2(d) \sim d^{-\gamma}, \tag{3}$$

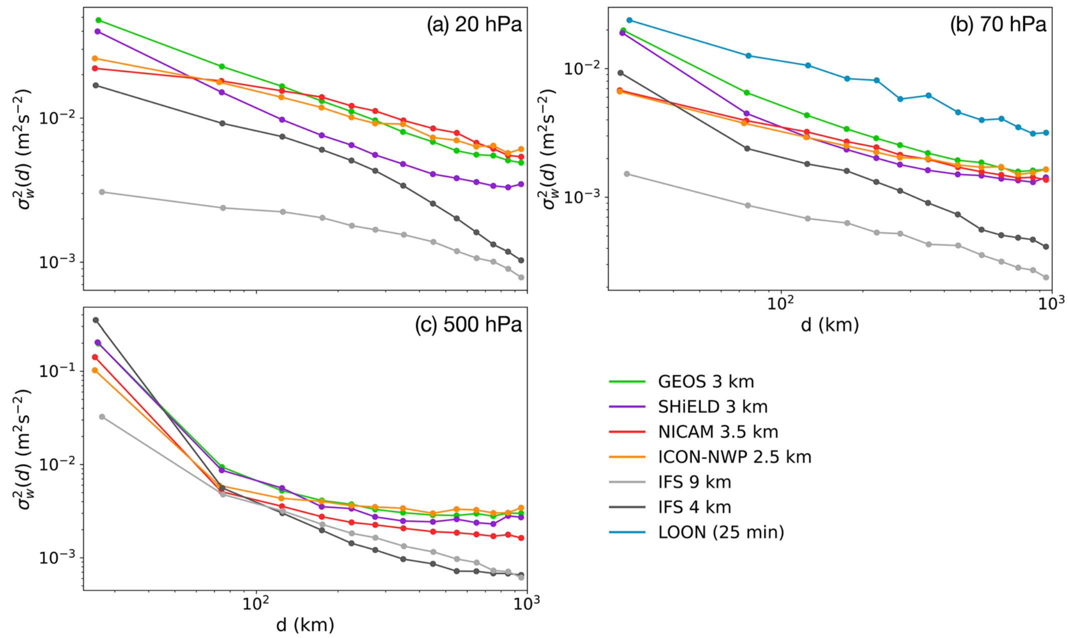

Figure 2. Variance of w as function of distance d to closest convection identified by precipitation rates larger than 6 mm hr^{-1} at (a) 20, (b) 70, and (c) 500 hPa. At 70 hPa, the blue curve corresponds to Loon with a low pass filtering time of 25 min.

with γ being the decay exponent ranging between 0.45 (ICON-NWP 2.5 km) and 1.08 (SHiELD 3 km) for different DYAMOND winter models at 70 hPa and 0.57 for Loon. In contrast to 500 hPa, we find no constant background for 20 and 70 hPa within 1,000 km. This is most likely explained by the lateral spreading of upward propagating gravity waves. The dependence of gravity wave amplitudes on distance to the source is greatest at the source levels and decreases with height due to lateral spreading. Thus, we find a power law decay in the whole regime at 70 and 20 hPa, although we can already observe the curves beginning to converge at large distances $d > 700$ km, in particular at 70 hPa.

For 500 hPa, $\sigma_w^2(d)$ decays strongly with increasing distance up to 200 km and then approaches a background value which corresponds to an additional constant $+c$ in Equation 3. The behavior of $\sigma_w^2(d)$ in the lower atmosphere, that is, 500 hPa, at short distances to convection, that is, $d \to 0$ km, can be understood by looking into differences in the precipitation rates in the models since in this region updrafts in convection contribute significantly to $\sigma_w^2(d \to 0)$. The box and whisker plots in Figure 3 show w as function of the co-located 15 min mean precipitation rate larger than 6 mm hr^{-1}. The green lines serve as a guide to the eye for an easier comparison between the different models showing the mean of GEOS 3 km. The blue histograms in the background show the distributions of precipitation rates larger than the threshold of 6 mm hr^{-1}. There are large differences between the models with respect to simulating precipitation as has been pointed out in Stephan et al. (2022).

IFS 9 km has the shortest tail in precipitation rates, and the least variations and mean values of w of all models consistent with Stephan et al. (2022). This is the case at all considered pressure levels, cf. Figure 2. The reason for the short tail in precipitation and the accompanied low mean values and variations of w is the parameterization of deep convection in IFS 9 km. In contrast, IFS 4 km does not parameterize deep convection. Accordingly, IFS 4 km has larger precipitation rates, and w as function of the precipitation rate shows larger mean values as well as larger variances away from precipitation pointing to larger gravity wave amplitudes. This agrees with IFS 4 km showing the largest value of $\sigma_w^2(d \to 0)$ at 500 hPa.

For the other models, $\sigma_w^2(d \to 0)$ at 500 hPa ranges in between the two IFS resolutions. This is consistent with the behavior of w and the precipitation rates presented in Figure 3. Except for NICAM 3.5 km, the maxima of the precipitation rate are larger than for IFS 4 km which points to a large number of deep convective gravity wave sources. However, the means and variances of w, and thus the wave amplitudes, are smaller than for IFS 4 km.

Although the w distribution of Loon was adjusted to the models by setting the filtering time T to 25 min, $\sigma_w^2(d)$ is larger than for the models, see Figure 2b. One reason for this is the difference of the observed precipitation rate

10.1029/2023JD038549

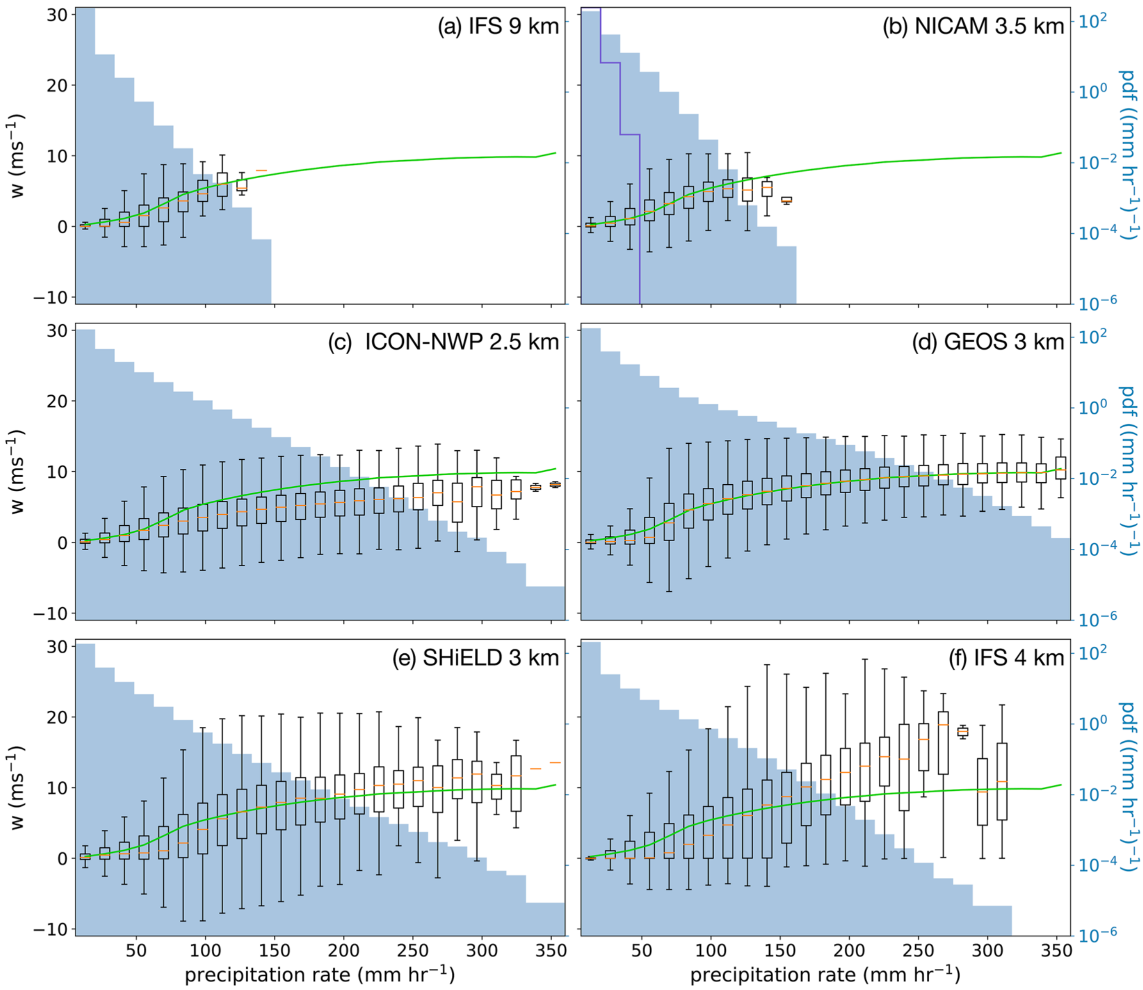

Figure 3. Dependence of w at 500 hPa on the local precipitation rate. The box and whisker plots represent the distribution of w as function of the precipitation rate. The orange lines show the medians. The boxes represent the first and third quartile. The whiskers correspond to the minimum (0th percentile) and maximum (100th percentile) values. We omit outliers for better clarity. The green line serves as a guide to the eye and represents the mean w values in Goddard Earth Observing System 3 km to ease the comparison between the models. The histograms in the background present the precipitation rate distributions. The purple histogram in panel (b) represents the precipitation rate distribution of CMORPH.

taken from CMORPH compared to the modeled ones. It is known that high-resolution models tend to overestimate rain rates and, in particular, find too many strong rain events as well as too much variance in the precipitation rates (Polichtchouk et al., 2022; Stephan et al., 2019a, 2019b). Figure 3 illustrates this for the DYAMOND winter simulations. The purple histogram in Figure 3b shows the distribution of precipitation rates larger than the threshold of 6 mm hr^{-1} from CMORPH. NICAM 3.5 km, which is the model presented in Figure 3b, tends to small precipitation rates when inter comparing the models as presented by the blue histograms. However, it yet has much larger precipitation rates than CMORPH. When comparing the number of grid points with precipitation rates larger than 6 mm hr^{-1}, we also find that it is larger for NICAM than for CMORPH. Figure 2 shows that for the same σ_w^2, the distance to convection is larger for the balloons than for the models. This is because we first adjusted the w distribution by choosing a filtering time of 25 min and second determined the distance to closest convection d using CMORPH. Together this leads to a shift of the variances σ_w^2 to larger distances d.

Having comparable precipitation rates for the different models and the observations would simplify the interpretation of $\sigma_w^2(d)$ with respect to gravity waves. However, it is not possible to use the same set of precipitation rates for the analysis because the dependence of σ_w^2 on the distance d comes from the fact that convection is a source of gravity waves. Thus, we can only study the correlation between σ_w^2 and the distance to closest convection d when using related data.

3.3. Gravity Wave Momentum Flux

In this last part of Section 3, we turn to the gravity wave momentum flux (GWMF) instead of the vertical velocity. We investigate the behavior as function of distance to closest convection d as in Corcos et al. (2021). Here, we restrict ourselves to the DYAMOND winter models. To study only the gravity wave contribution to the momentum flux, we separate the rotational and the divergent part of the horizontal wind field by a Helmholtz decomposition. Keeping only the divergent part leaves us approximately with the gravity wave horizontal wind field (Stephan et al., 2022). We remap the model output onto a N1024 Gaussian grid, perform the Helmholtz decomposition, and transform the divergent part back to the Gaussian N1024 grid. We do not reconstruct w since we expect the corrections to be small. In contrast to the horizontal winds, for which the divergent part is the smaller contribution, the vertical wind is dominated by gravity waves except in close vicinity to convection.

We consider the total vertical flux of horizontal momentum,

$$\mathcal{F} = \bar{\rho}\sqrt{\left(\overline{u'w'}\right)^2 + \left(\overline{v'w'}\right)^2}. \tag{4}$$

$\bar{x}$ is the background value of the quantity x and x' are deviations from this background, that is, $x' = x - \bar{x}$. The background value $\bar{x}$ is obtained by taking the average of x over a domain around the position of x with size 700×700 km^2. We thus calculate the background values for each point individually around its position which allows us to investigate the dependence on distances to convection closer than 700 km. We use the same randomly distributed virtual balloon points as before and calculate $\mathcal{F}$ for each balloon separately. The averaging step additionally to the Helmholtz decomposition is needed to remove wavelengths larger than 700 km which is the wavelength regime we restrict this analysis to. Figure 4 presents the mean and the variance of the GWMF for the DYAMOND winter models at (a and b) 20, (c and d) 70, and (e and f) 500 hPa.

Figures 4a, 4c, and 4e present the mean momentum flux. $\overline{\mathcal{F}}$ decays approximately exponentially with distance to convection, that is,

$$\overline{\mathcal{F}} = a\, e^{-d/d_0} + c. \tag{5}$$

The variable a determines the value at $d = 0$, d_0 is the exponential decay constant, and c is the background for $d \to \infty$. Except for IFS 9 km, the decay behavior of the different models is very similar which could be valuable for parameterizations. It also suggests that this aspect of GWMF properties may be learned with machine learning with the result being model independent, in contrast to amplitudes. For 20 hPa, we find a decay up to distances of 1,000 km with exponential decay constants d_0 between 422 for NICAM 3.5 and 214 km for ICON-NWP 2.5 km. At higher pressures, in particular at 500 hPa, we observe that the mean fluxes approach a constant background for large d. For 500 hPa, this background value ranges between 4.3 mPa for NICAM 3.5 and 2.9 mPa for SHiELD 3 km. For lower pressures, the background flux decreases and is between 1.6 mPa for NICAM 3.5 and 1.1 mPa for IFS 9 km at 70 hPa. The momentum fluxes in NICAM 3.5 km are larger than in the other models at all considered pressures and distances which is not the case for the variance of the vertical velocity, see Figure 2. This suggests different phase speed spectra.

Note that for most of the models, except for IFS 9 km, the three parameters a, d_0, and c are sufficient to describe the complete range of considered d. However, the value of d_0 depends on the averaging method, here over a 700 km square area. Distances d between 350 and 500 km mark the transition from convection being present within the 700×700 km^2 area to a convection free region. Therefore, the decay in this regime, described by d_0, depends on the choice for computing the average, in particular in the lower atmosphere where convection takes place, that is, at 500 hPa. Thus, the results at $d \lesssim 500$ km should be interpreted with care.

The waves propagate upwards away from their convective source. Therefore, they only reach large horizontal distances at sufficiently high altitudes. This may explain why a constant gravity wave background is only present at lower levels. A constant GWMF background has also been observed in the Strateole-2 data (Corcos et al., 2021). In this campaign, the superpressure balloons either drift in the tropical tropopause layer at approximately 70 hPa or in the lower stratosphere at about 55 hPa. In these measurements, the authors find a constant background flux of approximately 3 mPa (Corcos et al., 2021). For the DYAMOND winter models, we find it to be approximately 50% lower, that is, $\overline{\mathcal{F}}(d \to \infty) \lesssim 1.5$ mPa at 70 hPa. Some differences between observations and models are expected due to the fact that the models were running freely and evolved away from the initial state within the first few days. However, we do not expect this to have a systematic damping effect and thus it is unlikely to explain consistently smaller background values for all models. This seems to be consistent with our

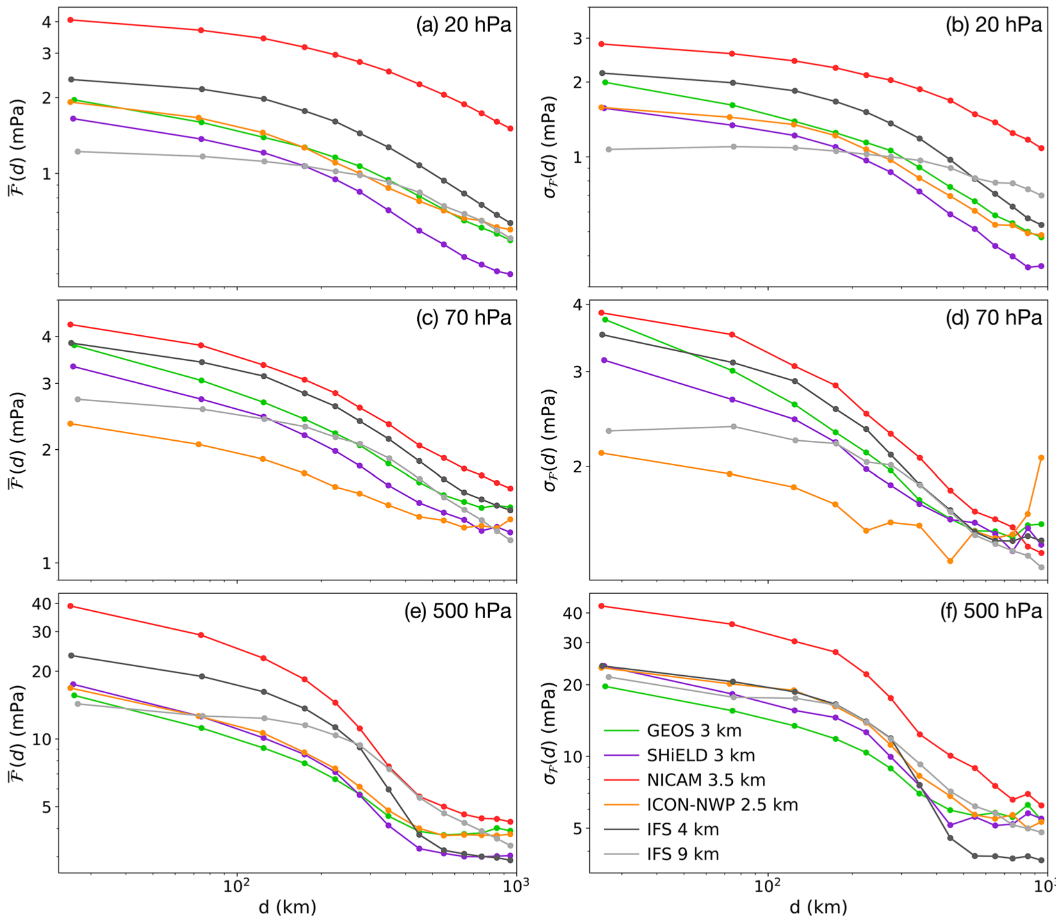

Figure 4. Gravity wave momentum flux, that is, total vertical flux of horizontal momentum, as function of distance to closest convection d. (a, c, and e) Show the mean flux and (b, d, and f) its variance at (a, b) 20, (c, d) 70, and (e, f) 500 hPa.

analysis of the variance of the vertical velocity in Section 3.2 where we find that at 70 hPa $\sigma_w^2(d)$ is larger for Loon than for the models.

Figures 4b, 4d, and 4f show the variances of the GWMFs. They behave very similarly to the mean flux. For higher pressures, we find the curves level out at constant backgrounds as for the mean flux. The exceptions to this behavior at large distances, for instance in the $\sigma_{\mathcal{F}}$ of ICON-NWP 2.5 km at 70 hPa, are most likely related to insufficient statistical sampling and should not be physically interpreted.

When comparing the dependence of σ_w^2 in Figure 2 and $\mathcal{F}$ in Figure 4 on distance to closest convection d, we find in all cases a convergence to the background for $d > 500$ km at 500 hPa and decays over the whole distance range of 1,000 km at 20 and 70 hPa. The absolute values of σ_w^2, $\overline{\mathcal{F}}$, and $\sigma_{\mathcal{F}}$ for $d \to 0$ are much larger at 500 hPa than at lower pressures which can be explained by strong updrafts in convective regions. However, the GWMF and its variance decay much faster, that is, exponentially, than σ_w^2, which decays like a power law.

Both the GWMF and the variance of w only approach constant backgrounds for large distances and high pressures. This highlights the limitation of parameterizations that do not condition their source level GWMF on actual sources but use constant background values instead. Moreover, the change in the shape of GWMF curves with height shows that lateral propagation may be important as well.

4. Summary and Outlook

In this paper, we compared some of the DYAMOND winter models to Loon superpressure balloon data in the tropics to assess the ability of the models to simulate gravity waves from convective sources. As a simple measure for gravity waves available from model output as well as from the observational data we used the variance of the vertical wind. For the models we also computed the gravity wave momentum flux. To study the propagation of waves, we considered these quantities as function of distance to closest convection similarly to what has been done in Corcos et al. (2021).

First, we looked into the distributions of the vertical velocity. We found that it follows approximately a normalized stretched exponential as introduced in Equation 2. The fit parameters, however, and thus the width of the distribution, vary at 70 hPa by a factor of 2 for α and a factor of 1.2 for β, respectively, for different models and Loon. For Loon, they depend on the filtering time of the low pass filter. We therefore used it as a tuning parameter to find a filtering time which corresponds to the effective model resolution. We found for GEOS 3 km an optimum filtering time of $T = 23$ min, for ICON-NWP 2.5 km $T = 25$ min, for SHiELD 3 km $T = 28$ min, and for NICAM 3.5 km $T = 30$ min. IFS was not included in the analysis because the appropriate filtering times are outside the considered range of T. The average distance a balloon travels is approximately four times the grid spacing for the time T that optimizes the match between the modeled and measured w distribution.

We then considered the variance of w as function of distance to closest convection d. To identify deep convection, we used precipitation rates larger than a threshold of 6 mm hr^{-1}. At low pressures, we found a power law decay with increasing d. At high pressures, the variance levels off at a constant background for large distances d. For small distances d at 500 hPa, we found that the value of σ_w^2 depends on the occurrence of large precipitation rates in the models as well as on the distribution of w as function of precipitation rates. At all pressure levels, the curves strongly depend on the amounts and maxima of modeled precipitation. At 70 hPa, we included Loon with a filtering time of 25 min in the analysis. We found larger values of $\sigma_w^2(d)$ for Loon. A main reason for this is that the observational precipitation rates taken from the satellite product CMORPH have less grid points with strong precipitation than in the models.

We finally calculated gravity wave momentum fluxes for the DYAMOND winter models. We did not include Loon here because for the approach we used, we needed global data coverage instead of trajectories. To restrict ourselves to gravity wave contributions, we performed a Helmholtz decomposition and kept only the divergent part of the horizontal wind field. Like for the variance of w, we considered the momentum flux as a function of distance to closest convection d. For 20 hPa, the mean momentum flux decays exponentially with d. For 70 and 500 hPa, we also found an exponential decay which quickly approaches a constant background. The background values found in DYAMOND are smaller than the one observed in the Strateole-2 campaign around 70 hPa. For the variance of the gravity wave momentum flux we found a similar behavior as for the mean.

Clearly, our results show differences in gravity wave amplitudes between the different models and observations. However, we find similar characteristics of the distributions of the vertical wind and the decay behavior with distance to closest convection of variances of w and gravity wave momentum fluxes which is promising for potential machine learning applications to understand the underlying physics.

To avoid unnecessary assumptions we here chose to compare models and observations in terms of quantities that minimize the level of required preprocessing. As a next step one could compute virtual balloon trajectories and condition not only on the distance to closest convection but also on more intricate measures for convection, such as convective organization and the wave propagation direction relative to convection. Here, we compared balloon trajectories to the global model output by introducing randomly distributed virtual balloon points and using the filtering time to coarsen the observational data using a 25 min time window. Given the relatively coarse model output frequency (1 hr or more), we believe this is the better choice, as the computation of trajectories would in this case not lead to reasonable results given the high frequencies of convectively generated gravity waves. Computation of trajectories during runtime would be ideal and allow making the best use of new and existing balloon data sets, although it would still require a statistical comparison in case of free-running models. It will be interesting to compare gravity wave signatures in storm-resolving models and superpressure balloons to new satellite techniques like ESA's EarthCARE which will be able to resolve vertical cloud motion and thus facilitate a comparison to data along trajectories.

Data Availability Statement

The Loon data are publicly available on Zenodo (Rhodes & Candido, 2021). Access to the DYAMOND winter data can be obtained via the ESiWACE coordination team, see https://www.esiwace.eu/services/dyamond-initiative for further information (ESiWACE & DKRZ, 2019).

AGU ADVANCING EARTH AND SPACE SCIENCES

Journal of Geophysical Research: Atmospheres

10.1029/2023JD038549

Acknowledgments

This research was funded by Schmidt Futures founded by Eric and Wendy Schmidt, as part of the Virtual Earth System Research Institute (VESRI). DYAMOND data management was provided by the German Climate Computing Center (DKRZ) and supported through the projects ESiWACE and ESiWACE2. The projects ESiWACE and ESiWACE2 have received funding from the European Union's Horizon 2020 research and innovation programme under Grants 675191 and 823988. This work used resources of the Deutsches Klimarechenzentrum (DKRZ) granted by its Scientific Steering Committee (WLA) under project IDs bk1040, bb1153, and bm1233. We thank our colleagues from the VESRI project DataWave for helpful discussions, suggestions, and ideas, in particular Ulrich Achatz, Joan Alexander, François Lott, and Riwal Plougonven. Open access funding enabled and organized by Projekt DEAL.

References

Alexander, M. J., & Holton, J. R. (1997). A model study of zonal forcing in the equatorial stratosphere by convectively induced gravity waves. *Journal of the Atmospheric Sciences*, *54*(3), 408–419. https://doi.org/10.1175/1520-0469(1997)054⟨0408:AMSOZF⟩2.0.CO;2

Anstey, J. A., Scinocca, J. F., & Keller, M. (2016). Simulating the QBO in an atmospheric general circulation model: Sensitivity to resolved and parameterized forcing. *Journal of the Atmospheric Sciences*, *73*(4), 1649–1665. https://doi.org/10.1175/JAS-D-15-0099.1

Atlas, R., & Bretherton, C. (2022). Aircraft observations of gravity wave activity and turbulence in the tropical tropopause layer: Prevalence, influence on cirrus and comparison with global-storm resolving models. *Atmospheric Chemistry and Physics Discussions*, *23*(7), 4009–4030. https://doi.org/10.5194/acp-2022-491

Banyard, T. P., Wright, C. J., Hindley, N. P., Halloran, G., Krisch, I., Kaifler, B., & Hoffmann, L. (2021). Atmospheric gravity waves in Aeolus wind lidar observations. *Geophysical Research Letters*, *48*(10), e2021GL092756. https://doi.org/10.1029/2021GL092756

Boccara, G., Hertzog, A., Vincent, R. A., & Vial, F. (2008). Estimation of gravity wave momentum flux and phase speeds from quasi-Lagrangian stratospheric balloon flights. Part I: Theory and simulations. *Journal of the Atmospheric Sciences*, *65*(10), 3042–3055. https://doi.org/10.1175/2008JAS2709.1

Bramberger, M., Alexander, M. J., & Grimsdell, A. W. (2020). Realistic simulation of tropical atmospheric gravity waves using radar-observed precipitation rate and echo top height. *Journal of Advances in Modeling Earth Systems*, *12*(8), e2019MS001949. https://doi.org/10.1029/2019MS001949

Bühler, O., Callies, J., & Ferrari, R. (2014). Wave–vortex decomposition of one-dimensional ship-track data. *Journal of Fluid Mechanics*, *756*, 1007–1026. https://doi.org/10.1017/jfm.2014.488

Callies, J., Ferrari, R., & Bühler, O. (2014). Transition from geostrophic turbulence to inertia–gravity waves in the atmospheric energy spectrum. *Proceedings of the National Academy of Sciences of the United States of America*, *111*(48), 17033–17038. https://doi.org/10.1073/pnas.1410772111

Cao, B., Haase, J. S., Murphy, M. J., Alexander, M. J., Bramberger, M., & Hertzog, A. (2022). Equatorial waves resolved by balloon-borne Global Navigation Satellite System radio occultation in the Strateole-2 campaign. *EGUsphere*, *22*(23), 15379–15402. https://doi.org/10.5194/egusphere-2022-381

Chen, Q., Ntokas, K., Linder, B., Krasauskas, L., Ern, M., Preusse, P., et al. (2022). Satellite observations of gravity wave momentum flux in the mesosphere/lower thermosphere (MLT): Feasibility and requirements. *Atmospheric Measurement Techniques Discussions*, *15*(23), 7071–7103. https://doi.org/10.5194/amt-2022-224

Christensen, H. M., & Driver, O. G. A. (2021). The fractal nature of clouds in global storm-resolving models. *Geophysical Research Letters*, *48*(23), e2021GL095746. https://doi.org/10.1029/2021GL095746

Conway, J. P., Bodeker, G. E., Waugh, D. W., Murphy, D. J., Cameron, C., & Lewis, J. (2019). Using project loon superpressure balloon observations to investigate the inertial peak in the intrinsic wind spectrum in the midlatitude stratosphere. *Journal of Geophysical Research: Atmospheres*, *124*(15), 8594–8604. https://doi.org/10.1029/2018JD030195

Corcos, M., Hertzog, A., Plougonven, R., & Podglajen, A. (2021). Observation of gravity waves at the tropical tropopause using superpressure balloons. *Journal of Geophysical Research: Atmospheres*, *126*(15), e2021JD035165. https://doi.org/10.1029/2021JD035165

Dinh, T., Podglajen, A., Hertzog, A., Legras, B., & Plougonven, R. (2016). Effect of gravity wave temperature fluctuations on homogeneous ice nucleation in the tropical tropopause layer. *Atmospheric Chemistry and Physics*, *16*(1), 35–46. https://doi.org/10.5194/acp-16-35-2016

ECMWF. (2020). IFS Documentation CY47R1 - Part III: Dynamics and numerical procedures. IFS Documentation CY47R1(3). https://doi.org/10.21957/u8ssd58

ESiWACE, & DKRZ. (2019). DYAMOND winter model output [Dataset]. Retrieved from https://www.esiwace.eu/services/dyamond-initiative

Espinosa, Z. I., Sheshadri, A., Cain, G. R., Gerber, E. P., & DallaSanta, K. J. (2022). Machine learning gravity wave parameterization generalizes to capture the QBO and response to increased CO_2. *Geophysical Research Letters*, *49*(8), e2022GL098174. https://doi.org/10.1029/2022GL098174

Haase, J. S., Alexander, M. J., Hertzog, A., Kalnajs, L., Deshler, T., Davis, S. M., et al. (2018). Around the world in 84 days. *Eos*, *99*. https://doi.org/10.1029/2018EO091907

Harris, L., Zhou, L., Lin, S.-J., Chen, J.-H., Chen, X., Gao, K., et al. (2020). GFDL SHiELD: A unified system for weather-to-seasonal prediction. *Journal of Advances in Modeling Earth Systems*, *12*(10), e2020MS002223. https://doi.org/10.1029/2020MS002223

Hindley, N. P., Wright, C. J., Gadian, A. M., Hoffmann, L., Hughes, J. K., Jackson, D. R., et al. (2021). Stratospheric gravity waves over the mountainous island of South Georgia: Testing a high-resolution dynamical model with 3-D satellite observations and radiosondes. *Atmospheric Chemistry and Physics*, *21*(10), 7695–7722. https://doi.org/10.5194/acp-21-7695-2021

Jensen, E. J., Ueyama, R., Pfister, L., Bui, T. V., Alexander, M. J., Podglajen, A., et al. (2016). High-frequency gravity waves and homogeneous ice nucleation in tropical tropopause layer cirrus. *Geophysical Research Letters*, *43*(12), 6629–6635. https://doi.org/10.1002/2016GL069426

Joyce, R. J., Janowiak, J. E., Arkin, P. A., & Xie, P. (2004). CMORPH: A method that produces global precipitation estimates from passive microwave and infrared data at high spatial and temporal resolution. *Journal of Hydrometeorology*, *5*(3), 487–503. https://doi.org/10.1175/1525-7541(2004)005⟨0487:CAMTPG⟩2.0.CO;2

Judt, F., Klocke, D., Rios-Berrios, R., Vanniere, B., Ziemen, F., Auger, L., et al. (2021). Tropical cyclones in global storm-resolving models. *Journal of the Meteorological Society of Japan. Ser. II*, *99*(3), 579–602. https://doi.org/10.2151/jmsj.2021-029

Lindborg, E. (2015). A Helmholtz decomposition of structure functions and spectra calculated from aircraft data. *Journal of Fluid Mechanics*, *762*, R4. https://doi.org/10.1017/jfm.2014.685

Lindgren, E. A., Sheshadri, A., Podglajen, A., & Carver, R. W. (2020). Seasonal and latitudinal variability of the gravity wave spectrum in the lower stratosphere. *Journal of Geophysical Research: Atmospheres*, *125*(18), e2020JD032850. https://doi.org/10.1029/2020JD032850

Lott, F., Rani, R., Podglajen, A., Codron, F., Guez, L., Hertzog, A., & Plougonven, R. (2023). Direct comparison between a non-orographic gravity wave drag scheme and constant level balloons. *Journal of Geophysical Research: Atmospheres*, *128*(4), e2022JD037585. https://doi.org/10.1029/2022JD037585

Massman, W. J. (1978). On the nature of vertical oscillations of constant volume balloons. *Journal of Applied Meteorology*, *17*(9), 1351–1356. https://doi.org/10.1175/1520-0450(1978)017<1351:otnovo>2.0.co;2

Miller, S. D., Straka, W. C., Yue, J., Smith, S. M., Alexander, M. J., Hoffmann, L., et al. (2015). Upper atmospheric gravity wave details revealed in nightglow satellite imagery. *Proceedings of the National Academy of Sciences of the United States of America*, *112*(49), E6728–E6735. https://doi.org/10.1073/pnas.1508084112

Morfa, Y. A., & Stephan, C. C. (2023). The relationship between horizontal and vertical velocity wavenumber spectra in global storm-resolving simulations. *Journal of the Atmospheric Sciences*, *80*(4), 1087–1105. https://doi.org/10.1175/JAS-D-22-0105.1

Nastrom, G. D. (1980). The response of superpressure balloons to gravity waves. *Journal of Applied Meteorology*, *19*(8), 1013–1019. https://doi.org/10.1175/1520-0450(1980)019<1013:trosbt>2.0.co;2

Nugent, J. M., Turbeville, S. M., Bretherton, C. S., Blossey, P. N., & Ackerman, T. P. (2022). Tropical cirrus in global storm-resolving models: 1. Role of deep convection. *Earth and Space Science*, *9*(2), e2021EA001965. https://doi.org/10.1029/2021EA001965

Podglajen, A., Hertzog, A., Plougonven, R., & Legras, B. (2016). Lagrangian temperature and vertical velocity fluctuations due to gravity waves in the lower stratosphere. *Geophysical Research Letters*, *43*(7), 3543–3553. https://doi.org/10.1002/2016GL068148

Polichtchouk, I., Wedi, N., & Kim, Y.-H. (2022). Resolved gravity waves in the tropical stratosphere: Impact of horizontal resolution and deep convection parametrization. *Quarterly Journal of the Royal Meteorological Society*, *148*(742), 233–251. https://doi.org/10.1002/qj.4202

Putman, W. M., & Lin, S.-J. (2007). Finite-volume transport on various cubed-sphere grids. *Journal of Computational Physics*, *227*(1), 55–78. https://doi.org/10.1016/j.jcp.2007.07.022

Rhodes, B., & Candido, S. (2021). Loon stratospheric sensor data [Dataset]. Zenodo. https://doi.org/10.5281/zenodo.5119968

Schoeberl, M. R., Jensen, E., Podglajen, A., Coy, L., Lodha, C., Candido, S., & Carver, R. (2017). Gravity wave spectra in the lower stratosphere diagnosed from project loon balloon trajectories. *Journal of Geophysical Research: Atmospheres*, *122*(16), 8517–8524. https://doi.org/10.1002/2017JD026471

Sharman, R. D., & Trier, S. B. (2019). Influences of gravity waves on convectively induced turbulence (CIT): A review. *Pure and Applied Geophysics*, *176*(5), 1923–1958. https://doi.org/10.1007/s00024-018-1849-2

Skamarock, W. C. (2004). Evaluating mesoscale NWP models using kinetic energy spectra. *Monthly Weather Review*, *132*(12), 3019–3032. https://doi.org/10.1175/MWR2830.1

Stephan, C. C., Duras, J., Harris, L., Klocke, D., Putman, W. M., Taylor, M., et al. (2022). Atmospheric energy spectra in global kilometre-scale models. *Tellus A: Dynamic Meteorology and Oceanography*, *74*, 280–299. https://doi.org/10.16993/tellusa.26

Stephan, C. C., Schmidt, H., Zülicke, C., & Matthias, V. (2020). Oblique gravity wave propagation during sudden stratospheric warmings. *Journal of Geophysical Research: Atmospheres*, *125*(1), e2019JD031528. https://doi.org/10.1029/2019JD031528

Stephan, C. C., Strube, C., Klocke, D., Ern, M., Hoffmann, L., Preusse, P., & Schmidt, H. (2019a). Gravity waves in global high-resolution simulations with explicit and parameterized convection. *Journal of Geophysical Research: Atmospheres*, *124*(8), 4446–4459. https://doi.org/10.1029/2018JD030073

Stephan, C. C., Strube, C., Klocke, D., Ern, M., Hoffmann, L., Preusse, P., & Schmidt, H. (2019b). Intercomparison of gravity waves in global convection-permitting models. *Journal of the Atmospheric Sciences*, *76*(9), 2739–2759. https://doi.org/10.1175/JAS-D-19-0040.1

Stevens, B., Satoh, M., Auger, L., Biercamp, J., Bretherton, C. S., Chen, X., et al. (2019). DYAMOND: The DYnamics of the Atmospheric general circulation Modeled On Non-hydrostatic Domains. *Progress in Earth and Planetary Science*, *6*(1), 61. https://doi.org/10.1186/s40645-019-0304-z

Tomita, H., & Satoh, M. (2004). A new dynamical framework of nonhydrostatic global model using the icosahedral grid. *Fluid Dynamics Research*, *34*(6), 357–400. https://doi.org/10.1016/j.fluiddyn.2004.03.003

Vincent, R. A., & Hertzog, A. (2014). The response of superpressure balloons to gravity wave motion. *Atmospheric Measurement Techniques*, *7*(4), 1043–1055. https://doi.org/10.5194/amt-7-1043-2014

Watanabe, S., Koshin, D., Noguchi, S., & Sato, K. (2022). Gravity wave morphology during the 2018 sudden stratospheric warming simulated by a whole neutral atmosphere general circulation model. *Journal of Geophysical Research: Atmospheres*, *127*(19), e2022JD036718. https://doi.org/10.1029/2022JD036718

Xie, P., Joyce, R., Wu, S., Yoo, S.-H., Yarosh, Y., Sun, F., & Lin, R. (2017). Reprocessed, bias-corrected CMORPH global high-resolution precipitation estimates from 1998. *Journal of Hydrometeorology*, *18*(6), 1617–1641. https://doi.org/10.1175/JHM-D-16-0168.1

Xie, P., Joyce, R., Wu, S., Yoo, S.-H., Yarosh, Y., Sun, F., & Lin, R. (2019). *NOAA CDR program (2019): NOAA climate data record (CDR) of CPC morphing technique (CMORPH) high resolution global precipitation estimates, version 1 (a) full resolution CMORPH data)*. NOAA National Centers for Environmental Information. https://doi.org/10.25921/w9va-q159[2021]

Zängl, G., Reinert, D., Rípodas, P., & Baldauf, M. (2015). The ICON (ICOsahedral Non-hydrostatic) modelling framework of DWD and MPI-M: Description of the non-hydrostatic dynamical core. *Quarterly Journal of the Royal Meteorological Society*, *141*(687), 563–579. https://doi.org/10.1002/qj.2378